J Mater Sci (2013) 48:5904–5916
DOI 10.1007/s10853-013-7386-6

Electrical transport in the ferromagnetic and paramagnetic state of potassium-substituted manganites $La_{1-x}K_xMnO_3$ ($x = 0.05$, 0.1 and 0.15)

Dinesh Varshney · Dinesh Choudhary · E. Khan

Received: 19 February 2013 / Accepted: 13 April 2013 / Published online: 25 April 2013
© Springer Science+Business Media New York 2013

Abstract We report the analysis of resistivity in the ferromagnetic and paramagnetic state of $La_{1-x}K_xMnO_3$ ($x = 0.05$, 0.10 and 0.15). The phonon frequencies are estimated from the ab initio theory with calibrated Hamiltonian for the atomic interaction between a pair such as Mn–O and La/K–O including van der Walls interaction. The modified electron–phonon (acoustic and optic) scattering incorporating the statistical factor and electron–electron and electron–magnon interactions is effective to describe the resistivity behaviour for a temperatures less than the metal–insulator transition (T_P) in the ferromagnetic state of $La_{1-x}K_xMnO_3$ ($x = 0.05$, 0.10 and 0.15). The Mott–Ioffe–Regel criterion for metallic conductivity is valid, and $k_F\ell \sim 1$, $\varepsilon_F\ \tau \sim 1$. Paramagnetic semiconducting resistivity is consistent with small polaron conduction model, and variable-range hopping is inappropriate for the description of resistivity behaviour in a high-temperature region, $T > T_P$. The results suggest that disorder-induced localisation of charge carriers dominates electrical transport.

Introduction

The manganites $La_{1-x}A_xMnO_3$ where La is a lanthanide and A is an alkaline-earth element have attracted much interest because of their characteristic magnetic and transport properties such as colossal magnetoresistance [1]. The above-mentioned properties have been explained by means of a double-exchange interaction between Mn^{3+} and Mn^{4+} [2] and electron–phonon interaction relating to Jahn–Teller-type lattice distortion of the MnO_6 octahedra to infer that the low- and high-temperature phases are a spin-polarised ferromagnetic metal and a polaronic paramagnetic insulator, respectively [3]. Lanthanum manganites doped with monovalent alkali metals such as Na^+, K^+ and Rb^+ show similar electrical and magnetic properties to divalent-doped manganites [4, 5].

Raman spectroscopy provided essential information about the lattice and JT distortion and orbital ordering in the manganites, which occur at variable doping levels [6]. In an ideal cubic ABO_3 perovskite, all atoms are at centrosymmetric sites and hence do not contribute to Raman modes. On the other hand, doping at La (A) or at Mn (B) site essentially causes a change in the structure and is due to either the mismatch of the ionic radii of the ions in the unit cell or due to the J–T effect associated with the Mn^{3+} ions. The result is the orthorhombic (*Pnma*) and the rhombohedral ($R3^{-}c$) structures, both of them presenting Raman-active phonons.

In reference to polaron participation, Millis et al. [7] suggest that for higher doping, the strong electron–phonon coupling localises the conduction band electrons as polarons; however, the polaronic effect is low as T which is decreased through Curie temperature T_C, permitting the formation of a metallic state. For doped manganites, it is pointed out that the electron–phonon interactions are substantial and the existence of insulating states competing with the DE-induced ferromagnetic metal is important. Besides, the ferromagnetic (FM) metallic phase, the antiferromagnetic (AF) charge-ordered insulating state is necessary to explain the CMR effect [8]. The antiferromagnetic super-exchange J_{AF} coupling plays a crucial role for the magnitude of the CMR effect. The J_{AF} is needed to stabilize the

D. Varshney (✉) · D. Choudhary · E. Khan
Materials Science Laboratory, School of Physics, Vigyan Bhawan, Devi Ahilya University, Khandwa Road Campus, Indore 452001, India
e-mail: vdinesh33@rediffmail.com

charge-ordered (CO) AF state that competes with the FM metal. The origin of the CMR effect relies on the nanometer-scale short-range order above T_C. To obtain CMR effects, clusters of just a few lattice spacings in size appear sufficient [9].

The parent compound $LaMnO_3$ is an antiferromagnetic insulator. Compounds of the series $La_{1-x}K_xMnO_3$ ($x = 0.05$, 0.10 and 0.15) exhibit resistance curves characteristic of a transition from a ferromagnetic–metallic to a paramagnetic–semiconducting state, as temperature increases. The transition temperature T_P is 239.8 K for $x = 0.05$, 261.9 K for $x = 0.1$ and 276 K for $x = 0.15$ [10]. The low-temperature ferromagnetic regime ($T < T_P$) shows metallic behaviour and the data have been fitted with different theoretical scattering mechanisms to describe the temperature dependence resistivity. From such a fitting, signatures of different types of interaction terms (viz., electron–electron, electron–magnon, or electron–phonon) are found to govern the transport mechanism in the low-temperature phase ($T < T_P$).

Earlier, Kumar and Majumdar solved the disordered Holstein double-exchange model to study the effect of disorder at strong electron–phonon coupling and noticed that even weak disorder enormously enhances the resistivity ρ at $T = 0$ K, simultaneously suppressing the density of states at the Fermi level. Furthermore, the presence of weak disorder suppresses the temperature-dependent increase of ρ and leads to a regime with $d\rho/dT < 0$ which is attributed to the disorder-induced tendency towards polaron formation [11]. Later on, it was demonstrated that the extrinsic disorder controls the interplay of lattice polaron effects and spin fluctuations and leads to widely varying regimes in transport explicitly for optimally doped manganites [12].

We may refer to the work of Alexandrov et al. [13] which states that polarons behave like heavy particles and can be mobile with metallic conduction at low temperatures and form a polaronic Fermi liquid. The resistivity data of $La_{1-x}Ca_xMnO_3$ below 100 K are consistently retraced by a polaron mechanism. Later on, Zhao et al. [14] showed that the behaviour of resistivity at low temperature is consistent with small polaron coherent motion that involves a relaxation due to a low-lying optical phonon mode.

At low temperatures, a dominant T^2 contribution in resistivity is generally observed and has been ascribed to electron–electron scattering [15, 16]. Jaime et al. [17] have shown that the resistivity is essentially temperature independent below 20 K and exhibits a strong T^2 dependence above 50 K. Kubo and Ohata [18] suggest that two-magnon processes predict a leading $T^{9/2}$ dependence of the resistivity. Alexandrov and Bratkovsky argued that the resistivity peak and the colossal magnetoresistance of hole-doped manganites $La_{0.75}Ca_{0.25}MnO_3$ are a result of the current carrier density collapse with strong electron–phonon coupling. The ferromagnetic transition in manganites is driven by an exchange interaction of polaronic carriers with localised spins [19]. Earlier, we noticed that in $La_{0.67}Ca_{0.33}MnO_3$, an additional contribution arising from the electron–electron contribution is a must to analyse the ferromagnetic metallic resistivity behaviour [20]. This suggests that the electron–phonon, electron–electron and electron–magnon scatterings must be important causes of resistivity in the metallic state.

In order to explain the high-temperature electrical transport properties, two distinct phenomena based on two different models, viz., variable-range hopping (VRH) [21] and small polaron conduction (SPC) [22], were tested. We may refer to the work of Jaime et al. who suggested that doping at the Mn site influences the polaronic transport as it causes a change in the polaron-hopping distance and also the polaron concentration [23]. Ang et al. [24] showed that for $T > T_P$, the resistivity data of their Co-doped bilayer manganites $LaSr_2Mn_2O_7$ could fit well using the VRH model and the SPC model and also using the thermally activated conduction law.

The present investigations are structured as follows. In the "Method of computation" section, we first formulate an effective interionic interaction potential, which includes the long-range Coulomb, van der Waals (vdW) interaction and the short-range repulsive interaction up to second-neighbour ions within the Hafemeister and Flygare approach. This enables us to compute the Debye and Einstein temperatures of $La_{1-x}K_xMnO_3$ ($x = 0.05$, 0.1 and 0.15). We employ the Bloch–Gruneisen (BG) method to estimate both the independent contributions of acoustic and optical phonons and their combined effects. For the semiconducting region, we compute resistivity behaviour with Mott's VRH and SPC. The small polaron model takes care of the coherent motion of charge carriers and involves a relaxation due to a low-lying optical phonon mode. Details of the numerical analysis and its results are discussed in the "Discussion and analysis of results" section.

The main findings for K-substituted manganites include the following:

(a) The estimated Debye and Einstein temperatures from the ab initio theory for the atomic interaction including van der Walls interaction are consistent with the experimental results;
(b) the optical phonons yield a relatively larger contribution to the resistivity compared to the contribution of acoustic phonons;
(c) the modified electron–phonon model of resistivity partially retraces the reported metallic resistivity behaviour in the temperature range $T < T_P$ for $La_{1-x}K_xMnO_3$ ($x = 0.05$, 0.1 and 0.15);

(d) the quadratic temperature dependence of $\rho_{\text{diff.}}$ [= $\rho_{\text{exp.}} - \{\rho_0 + \rho_{\text{e-ph}}]$ is interpreted in terms of 3D electron–electron inelastic scattering;
(e) the $T^{4.5}$ dependence due to electron–magnon scattering is further required for a complete explanation;
(f) the Mott–Ioffe–Regel criterion for metallic conductivity is valid, $k_{F\ell} \sim 1$ and $\varepsilon_F \tau \sim 1$;
(g) the VRH model is inappropriate for description of resistivity behaviour in high-temperature region, $T > T_P$; and
(h) the SPC model consistently explains higher temperature resistivity behaviour ($T > T_P$).

A summary and our main conclusions are presented in the "Conclusion" section.

Method of computation

Raman spectroscopy provides information about the electronic and lattice processes responsible for the physical behaviour of the mixed valence manganites [25]. The ideal perovskite ABO_3 of cubic structure presents around 15 normal modes of vibration. The lowest frequency (external mode) corresponds to a vibration of the A ions against the rigid BO_6 octahedra. The intermediate frequency (bending mode) corresponds to a vibration where the B ion and two apical oxygens move against the other four oxygens of the octahedron. At the highest frequency (stretching mode), the B ion moves against the rigid oxygen octahedron [26]. We can thus model the phonon spectrum consisting of an acoustic branch of the Debye type and a separated optical peak with characteristic Einstein temperature.

The understanding of the dynamical properties of materials requires the formulation of an effective interionic potential. To begin with, we made the following assumptions: the change in force constants is small; the short-range interactions are effective up to the second-neighbour ions; and the atoms are held together by harmonic elastic forces without any internal strains within the crystal. We thus express the crystal energy for a particular lattice separation (r) as

$$U(r) = U_C(r) + U_R(r) + U_V(r) \tag{1}$$

The first term is the Coulomb energy with α_m as the Madelung constant [27] as follows:

$$U_C(r) = -\sum_{ij} \frac{Z_i Z_j e^2}{r_{ij}} = -\frac{\alpha_m Z^2 e^2}{r} \tag{2}$$

Here, r_{ij} is the separation distance between i (j) ions.

The short-range overlap repulsive energy following Hafemeister and Flygare [28] is the second term in Eq. (1) and is

$$U_R(r) = nb\beta_{ij} \exp\left(\frac{r_i + r_j - r_{ij}}{\rho}\right) + n' b\beta_{ii} \exp\left(\frac{2r_i - kr_{ij}}{\rho}\right) + n' b\beta_{jj} \exp\left(\frac{2r_j - kr_{ij}}{\rho}\right) \tag{3}$$

The ionic radii are r_i and r_j, k is the structure factor and $n(n')$ is the number of nearest (next nearest) ions. Further, the notations b and ρ denote the hardness and range parameters, respectively.

The Pauling coefficients, β_{ij}, are defined in terms of valence [Z_i (Z_j)] and the number of the outermost electrons [n_i (n_j)] in the anions (cations) as

$$\beta_{ij} = 1 + (Z_i/n_i) + (Z_j/n_j) \tag{4}$$

The last term in Eq. (1) is the vdW energy, denoted as

$$U_V(r) = -\left(\sum_{ij} \frac{c_{ij}}{r_{ij}^6} + \sum_{ij} \frac{d_{ij}}{r_{ij}^8}\right) \tag{5}$$

$$= -\left(\frac{C}{r^6} + \frac{D}{r^8}\right) \tag{6}$$

due to dipole–dipole (d–d) and dipole–quadruple (d–q) interactions. The abbreviations C and D represent overall vdW coefficients due to interactions mentioned in Eq. (1), defined as [27]

$$C = c_{ij} S_6(r) + \frac{1}{2}(c_{ii} + c_{jj}) S_6(0) \tag{7}$$

and

$$D = d_{ij} S_8(r) + \frac{1}{2}(d_{ii} + d_{jj}) S_8(0) \tag{8}$$

c_{ij} and d_{ij} are the vdW coefficients due to d–d and d–q interactions. We follow the variational method [29] to derive c_{ij} and d_{ij} as

$$c_{ij} = \frac{3}{2} \frac{e\hbar}{\sqrt{m_e}} \alpha_i \alpha_j \left[(\alpha_i/N_i)^{1/2} + (\alpha_j/N_j)^{1/2}\right]^{-1} \tag{9}$$

and

$$d_{ij} = \frac{27}{8} \frac{\hbar^2}{m} \alpha_i \alpha_j \left[(\alpha_i/N_i)^{1/2} + (\alpha_j/N_j)^{1/2}\right]^2 \times \left[(\alpha_i/N_i) + \frac{20}{3}(\alpha_i \alpha_j / N_i N_j)^{1/2} + (\alpha_j/N_j)\right]^{-1}. \tag{10}$$

Here, m_e is the electron mass, α_i is the electronic polarisability and N_i denotes the effective number of electrons of the ith ion. The values of the overall vdW coefficients are

obtained using Eqs. (7) and (8) and weighted in terms of appropriate lattice sums [$S_6(0)$, $S_6(r)$, $S_8(0)$ and $S_8(r)$] [27]. The individual vdW coefficients c_{ij} and d_{ij} are obtained with certainty and accuracy as the excitation energies are ignored in Eqs. (9) and (10).

Herein, we shall seek the interionic interaction between a pair such as Mn–O and La/K–O. It is clear from the above descriptions that the present effective interionic potential contains only two free parameters (b and ρ), which are determined from the equilibrium conditions

$$\left(\frac{\mathrm{d}U}{\mathrm{d}r}\right)_{r=r_0} = 0 \tag{11}$$

and bulk modulus

$$B_{\mathrm{T}} = \frac{1}{9kr_0}\left(\frac{\mathrm{d}^2U}{\mathrm{d}r^2}\right)_{r=r_0}. \tag{12}$$

The model parameters obtained from Eqs. (11) and (12) have been used to compute the second-order elastic constants (SOECs) (C_{11}, C_{12} and C_{44}) as [30–33]

$$C_{11} = \frac{e^2}{4r_0^4}\left[-5.112Z_{\mathrm{m}}^2 + A_1 + \frac{(A_2+B_2)}{2}\right], \tag{13}$$

$$C_{12} = \frac{e^2}{4r_0^4}\left[0.226Z_{\mathrm{m}}^2 - B_1 + \frac{(A_2-5B_2)}{2}\right], \tag{14}$$

$$C_{44} = \frac{e^2}{4r_0^4}\left[2.556Z_{\mathrm{m}}^2 + B_1 + \frac{(A_2+3B_2)}{4}\right], \tag{15}$$

where (A_1, B_1) and (A_2, B_2) are the short-range parameters for the nearest and the next nearest neighbours, respectively. These parameters are defined as

$$A_1 = \frac{4r_0^3}{e^2}\left[\frac{\mathrm{d}^2}{\mathrm{d}r^2}V_{ij}(r)\right]_{r=r_0}, \tag{16}$$

$$A_2 = \frac{4(r_0\sqrt{2})^3}{e^2}\left[\frac{\mathrm{d}^2}{\mathrm{d}r^2}V_{ii}(r) + \frac{\mathrm{d}^2}{\mathrm{d}r^2}V_{jj}(r)\right]_{r=r_0\sqrt{2}}, \tag{17}$$

$$B_1 = \frac{4r_0^3}{e^2}\left[\frac{\mathrm{d}}{\mathrm{d}r}V_{ij}(r)\right]_{r=r_0}, \tag{18}$$

$$B_2 = \frac{4(r_0\sqrt{2})^2}{e^2}\left[\frac{\mathrm{d}}{\mathrm{d}r}V_{ii}(r) + \frac{\mathrm{d}}{\mathrm{d}r}V_{jj}(r)\right]_{r=r_0\sqrt{2}} \tag{19}$$

where $V_{ij}(r)$ is the short-range potential between the ions as follows:

$$V_{ij}(r) = b\beta_{ij}\exp\left(\frac{r_i + r_j - r_{ij}}{\rho}\right) + c_{ij}r_{ij}^{-6} + d_{ij}r_{ij}^{-8}. \tag{20}$$

The elastic force constant κ is derived at the equilibrium interionic distance r_0 following

$$\kappa = \frac{r_0}{2}\left[\pi^2(C_{11}-C_{12})(C_{11}+C_{12}+2C_{44})(C_{44})\right]^{\frac{1}{5}}. \tag{21}$$

Thus, we have estimated the elastic force constants in terms of the developed potential for a pair such as Mn–O and La/K–O and the total elastic force constants of the K-doped $LaMnO_3$. This continuum model thus takes care of the clear physical binding in doped manganites. We stress that the analytical model incorporating realistic interactions can describe those cohesive properties of such solids that depend on vdW interactions. However, the true potential must recognize the correct charge distribution and the relative orientations of the interacting atoms in manganites, which is a complicated task.

We shall now estimate the acoustic Debye branch characterized by the Debye temperature θ_{D} and an optical peak defined by the Einstein temperature θ_{E}. The Debye frequency is characterized as a cut-off frequency at the Brillouin zone boundary. It can be expressed in terms of effective value of ionic mass and elastic force constant for crystal lattices with two different kinds of atoms such as Mn–O and La/K–O, which we deal with. The acoustic-mode and optical-mode frequencies are estimated in an ionic model using a value of effective ion charge $Ze = -2e$.

We choose an acoustic mass $M = (2M_+ + M_-)$ [Mn(O) which is symbolized by M_+ (M_-)], $\kappa^* = 2\kappa$, for each directional oscillation mode to get the acoustic phonon frequency as [20]

$$\omega_{\mathrm{D}} = \sqrt{\frac{2\kappa^*}{M}}. \tag{22}$$

In this regard, for a pair-wise potential, the phonons are optic in origin and the frequency is determined by the reduced mass of the pair as $\mu^{-1} = M(A)^{-1} + M(B)^{-1}$ where A is the anion (La/K, Mn) and B is the cation (O)

$$\omega_{\mathrm{LO}}^2 = \frac{\kappa+\alpha}{\mu}, \tag{23}$$

$$\omega_{\mathrm{TO}}^2 = \frac{\kappa-\alpha}{\mu}, \tag{24}$$

where α is the force constant as

$$\alpha = \frac{8\pi}{3}\frac{(Ze)^2}{\Omega}, \tag{25}$$

ω_{LO} (ω_{TO}) symbolized the longitudinal (transverse) optical phonon frequency and Ω is the volume of the unit cell.

To formulate a specific model, we start with the general expression for the temperature-dependent part of the resistivity, given by

$$\rho = \frac{3\pi}{\hbar e^2 v_F^2} \int_0^{2k_f} |v(q)|^2 \left\langle |S(q)|^2 \right\rangle \left(\frac{1}{2k_F}\right)^4 q^3 \mathrm{d}q. \tag{26}$$

$v(q)$ is the Fourier transform of the potential associated with one lattice site and $S(q)$ is the structure factor, and following the Debye model, it takes the following form:

$$|S(q)|^2 \approx \frac{k_B T}{M v_s^2} f(\hbar\omega/k_B T) \tag{27}$$

$$f(x) = x^2 [e^x - 1]^{-1} [1 - e^{-x}]^{-1} \tag{27a}$$

Using

$$[e^x - 1]^{-1} [1 - e^{-x}]^{-1} = e^{-x} [1 - e^{-x}]^{-2} \tag{27b}$$

to get

$$f(x) = x^2 e^{-x} [1 - e^{-x}]^{-2} \tag{28}$$

$f(x)$ represents the statistical factor. Thus, the resistivity expression leads to

$$\rho \approx \left(\frac{3}{\hbar e^2 v_F^2}\right) \frac{k_B T}{M v_s^2} \int_0^{2k_F} |v(q)|^2 \times \left[\frac{(\hbar\omega/k_B T)^2 q^3 \mathrm{d}q}{(\exp(\hbar\omega/k_B T) - 1)(1 - \exp(-\hbar\omega/k_B T))}\right]. \tag{29}$$

v_s being the sound velocity. The acoustic phonon contribution to resistivity leads:

$$\rho_{ac}(T, \theta_D) = 4A_{ac}(T/\theta_D)^4 \times T \int_0^{\theta_D/T} x^5 (e^x - 1)^{-1} (1 - e^{-x})^{-1} \mathrm{d}x \tag{30}$$

where $x = \hbar\omega/k_B T$. A_{ac} is a constant of proportionality, defined as

$$A_{ac} \cong \frac{3\pi^2 e^2 k_B}{k_F^2 v_s^2 L \hbar v_F^2 M} \tag{31}$$

We may add that the temperature dependence of resistivity within the BG framework follows [34]

$$\rho(T, \theta_D) = \frac{c}{\theta_D} \left(\frac{T}{\theta_D}\right)^m J_m \left(\frac{T}{\theta_D}\right) \tag{32}$$

where c is a constant, θ_D is the Debye temperature of the conventional metal and T is the absolute temperature. Here, the index m takes integer and non-integer values. The generalized BG function follows

$$J_m \left(\frac{T}{\theta_D}\right) = \int_0^{\theta_D/T} \frac{x^m e^{-x}}{(1 - e^{-x})^2} \mathrm{d}x \tag{33}$$

For non-integer values m in the range of 3–5, one can obtain the best-fitting curve which resembles the experimental $\rho(T)$ data.

It is known to us that in the metallic state, the electron–phonon, electron–electron, electron–magnon scattering and polaronic effects are the major proponents of various conceptions in electrical transport. As the resistivity is additive, if the Matthiessen rule is obeyed, the resistivity is represented as a sum $\rho\ (T) = \rho_0 + \rho_{e\text{-}ph}\ (T)$, where ρ_0 is the residual resistivity that does not depend on temperature as electrons also scatter off impurities, defects and disordered regions. However, in the case of the Einstein type of phonon spectrum (an optical mode), $\rho_{op}\ (T)$ may be described as follows:

$$\rho_{op}(T, \theta_E) = A_{op} \theta_E^2 T^{-1} \left[e^{\theta_E/T} - 1\right]^{-1} \left[1 - e^{-\theta_E/T}\right]^{-1}, \tag{34}$$

A_{op} is defined in an analogous manner to Eq. (31).

We have thus modified the electron–phonon scattering contribution to resistivity by incorporating the statistical factor in the ferromagnetic metallic state by combining both terms arising from acoustic and optical phonons:

$$\rho_{e-ph}(T) = \rho_{ac}(T, \theta_D) + \rho_{op}(T, \theta_E). \tag{35}$$

Henceforth, the total resistivity is as follows:

$$\begin{aligned} \rho(T, \theta_D, \theta_E) &= \rho_0 + \rho_{ac}(T, \theta_D) + \rho_{op}(T, \theta_E) \\ &= \rho_0 + 4A_{ac}(T/\theta_D)^4 T \\ &\quad \times \int_0^{\theta_D/T} x^5 (e^x - 1)^{-1} (1 - e^{-x})^{-1} \mathrm{d}x\ . \\ &\quad + A_{op} \theta_E^2 T^{-1} [\exp(\theta_E/T - 1)]^{-1} \\ &\quad \times [1 - \exp(-\theta_E/T)]^{-1} \end{aligned} \tag{36}$$

In order to analyse the resistivity data of the high-temperature region, $T > T_P$, we have made a computation following model I, VRH, and model II, adiabatic SPC. In the high-temperature range, for example, in the paramagnetic semiconducting state, we have fitted the resistivity data using the VRH model. The expression as derived by Mott for conductivity follows [15, 16, 42]

$$\sigma = \sigma_{oh} \exp(-T_0/T)^{0.25}. \tag{37}$$

with σ_{oh} as a constant and T_0 defined in terms of the density of state in the vicinity of Fermi energy $N(\varepsilon_F)$ and the localisation length a as

$$T_o = \frac{18}{k_B N(\varepsilon_F) a^3}, \tag{38}$$

T_0 describes the hopping transport in doped manganites where the carriers are localised by random potential fluctuations and the preferred hopping is between sites lying within a certain range of energy.

We shall briefly sketch the description of resistivity in the temperature range $T > T_P$ due to model II. It is worth mentioning that the most rapid motion of a small polaron occurs when the carrier hops each time the configuration of vibrating atoms in an adjacent site coincides with that in the occupied site. Henceforth, the charge carrier motion within the adiabatic regime is faster than the lattice vibrations and the resistivity for SPC is as follows [15, 16, 43]:

$$\rho = \rho_{os} T \exp\left(\frac{E_P}{k_B T}\right), \tag{39}$$

E_P is the polaron formation energy and k_B is Boltzmann constant. The resistivity coefficient ρ_{os} is given by

$$\rho_{os} = \frac{k_B}{n(1-x)e^2 D}. \tag{40}$$

Here, n is the charge carrier density ($\sim 10^{20}$ cm^{-3}), x is the hole (Mn^{4+}) content, e, the electronic charge and D is the polaron diffusion constant. The polaron diffusion constant for a typical cubic coordination can be given explicitly as $D = a^2\nu/6$ where a is the lattice constant and ν is the characteristic frequency of the longitudinal optical phonon that carries polaron through the lattice.

The parent $LaMnO_3$ at high temperatures is an insulator with a cubic structure and becomes tetragonal due to distortions at low temperatures. Doping at a La site by Ca, Sr, Ba, Na, K and so forth leads to a decrease not only in the structural phase transition temperature but also in the overall behaviour of resistivity. However, for optimized doped $x \cong 0.3$, the material is still insulating (at about room temperature and higher) and the resistivity is much higher than the Mott limit [15, 16, 43]. The substitution at the La site by divalent (monovalent) ions changes the valence of the Mn site as the outer Mn d-orbital shows twofold degeneration and the result is Jahn–Teller (breathing type) distortion of the oxygen octahedra focused at each of the Mn-occupied (unoccupied) sites. The energy required for the formation of a local lattice distortion is about 0.6 eV per site. Identifying a strong electron–phonon coupling, and hence polaronic transport, is essential in the doped materials. At high temperatures, the Jahn–Teller distortions are decorrelated, but do not disappear [35].

On the other hand, the double-exchange mechanism shows that the oxygen ion is closed shell and supports hopping. In the true sense, an electron jumps onto a Mn ion on the right simultaneously as an electron hops onto the O ion from the Mn on the left. Henceforth, in the double hopping, both hopping electrons should have the same spin via the oxygen (O^{2-}) ions. Following Hund's rule, the Mn^{3+} and Mn^{4+} ions should have the electron parallel the spin moments for hopping. This mechanism connects the parallel alignment of Mn moments (ferromagnetism) with hopping of carriers (metallic conduction). Thus, the effective positive exchange coupling induced by the carriers was known as double exchange.

Actually, the lattice vibration of O ions essentially pushes the electrons towards vacant states in the Mn ion inducing a local distortion of the lattice. Such self-trapping of the charge carriers is substantial above the Curie temperature. However, below the Curie temperature, the self-trapping disappears because the bandwidth broadens and the electrons are much more mobile. It is inferred that at a high temperature, the effective positive exchange coupling induced by the carriers does not solely contribute to the resistivity and that a strong electron phonon interaction arising from the Jahn–Teller splitting of the outer Mn d level is essentially required [36].

Discussion and analysis of results

Any discussion of the mixed-valent oxides necessitates the knowledge of the structural aspects, and this is particularly true of the calculations reviewed here. Also, applying the available information on the developed theory inevitably entails certain complications and one has to find suitable data that vary from technique to technique. Special attention is paid in this approach to address the issue of whether long-range or short-range interactions are at the origin of the transport properties of the divalent K-doped manganites. The effective interionic potential is thus constructed in an easily generalisable manner with a realistic value of the structural parameters, which actually control the resistivity behaviour. The values of Debye and Einstein temperature have been computed using the values of the two model parameters, namely range (ρ) and hardness (b), for a pair such as La/K–O and Mn–O, which has been evaluated from the experimental values of equilibrium distance and bulk modulus.

The values of the overall vdW coefficients C and D involved in Eqs. (7) and (8) have been evaluated from the well-known Slater–Kirkwood variational methods [29] which are listed in Table 1. We use the A site ionic radii (La/K) as 1.514 Å. Within the continuum model, we notice that the hardness parameter (b_1 and b_2) decreases and the range parameter (ρ_1 and ρ_2) decreases with the increased K doping concentration (x) in hole-doped $La_{1-x}K_xMnO_3$. The model parameters and the SOECs are illustrated in Table 2. The elastic force constant κ is derived at the equilibrium interionic distance r_0 following Eq. (21). The calculated values of κ are 5.767×10^5, 5.775×10^5 and

Table 1 Van der Waals coefficients of $La_{1-x}K_xMnO_3$ ($x = 0.05, 0.1, 0.15$) (c_{ij} in units of 10^{-60} ergcm^6 and d_{ij} in unit of 10^{-76}ergcm^8)

x		c_{ii}	c_{ij}	c_{jj}	C	d_{ii}	d_{ij}	d_{jj}	D
	Mn–O	120.18	180.39	270.87	1543	131.53	193.35	284.10	1355
$x = 0.05$	La/K–O	12.75	56.99	270.87	632.09	19.42	74.58	284.10	579.8
$x = 0.1$	La/K–O	12.21	55.06	270.87	618.88	18.43	71.53	284.10	560.6
$x = 0.15$	La/K–O	11.67	53.13	270.87	605.66	17.44	68.48	284.10	541.5

Table 2 The model parameters (b, ρ) and the second-order elastic constants for $La_{1-x}K_xMnO_3$ ($x = 0.05, 0.1, 0.15$) samples

x	Model parameters				Second-order elastic constants		
	b_1 (La/K–O) (10^{-12} erg)	ρ_1 (La/K–O) (Å)	b_2 (Mn–O) (10^{-12} erg)	ρ_2 (Mn–O) (Å)	C_{11} (10^{12} dyne cm^{-2})	C_{12} (10^{12} dyne cm^{-2})	C_{44} (10^{12} dyne cm^{-2})
0.05	75.9	26.7	5.39	33.7	7.79	3.65	2.57
0.1	71.8	26.7	5.39	33.7	7.97	3.66	2.57
0.15	67.5	26.7	5.37	33.6	8.04	3.71	2.62

5.838×10^5 g ms^{-2} for $x = 0.05$, 0.1 and 0.15, respectively. Due to a lack of other theoretical calculations, the deduced value of the model force constant could not be compared. Nevertheless, the evaluation of the elastic force constant gives a valuable guide to the behaviour of vdW-type forces in predicting the model phonon energies. Yet, the goal is not to determine the manner in which such interactions lead to the description of phonon frequencies, but to discuss the electrical resistivity behaviour.

Finally, we evaluate the values of acoustic and optical phonon frequency (ω_D, ω_{LO} and ω_{TO}) corresponding to Debye and Einstein temperature. The computed values of ω_D, ω_{LO} and ω_{TO} are presented in Table 3. We must mention that these computed values of ω_D, ω_{LO} and ω_{TO} for $La_{1-x}K_xMnO_3$ with ($x = 0.05$, 0.1 and 0.15) could not be compared due to the lack of experimental data. However, the computed values of the Debye and Einstein temperature for $La_{0.7}Ba_{0.3}MnO_3$ and other manganites following the EIoIP approach yield consistent results with the available experimental results [37–41].

It is true that the two-orbital model based on Wannier functions predicts the electronic states such as charge ordering in manganites. It is pointed out by Marzari et al. [42] that the Wannier function approach of the electronic problem is useful for the description of electron dynamics following semi-classical theory as well as the magnetic interactions in solids. In the present investigation, we do not intended to discuss the electron dynamics as well the magnetic interactions, but focused on determining the acoustic (optical) phonon frequency to estimate the electron–phonon contribution of resistivity in the ferromagnetic metallic phase.

The developed effective interionic interaction potential takes care of the interactions between a pair such as Mn–O and La/K–O. The interactions thus are attractive Coulomb and vdW as well as a short-range overlap repulsive interaction following Hafemeister- and Flygare-type potential. The advantage of using this potential is that it takes care of a number of nearest (next nearest) ions, the valence and a number of the outermost electrons in the anions (cations). Thus, it takes care of the structural parameters that yield an approximately correct description of the interactions between a pair such as Mn–O and La/K–O. Henceforth, we will estimate the acoustic (optical) phonon frequency consistent with the Raman measurements to estimate the electron–phonon contribution of resistivity.

We must refer to the work of Millis [35] who determined the elastic parameters using a mean field approximation with emphasis on Mn–O bond lengths and evaluated Mn–Mn and Mn–O force constants for the lattice

Table 3 Parameters obtained corresponding to the best fit to the experimental data of $La_{1-x}K_xMnO_3$ ($x = 0.05, 0.1, 0.15$) samples by using BG model

x	T_P (K)	ω_D (meV)	ω_{LO} (meV)	ω_{TO} (meV)	Parameters obtained from BG model		
					ρ_0 (Ω cm)	$A_{ac} \times 10^{-4}$ (Ω cm K^{-1})	$A_{op} \times 10^{-3}$ (Ω cm K^{-1})
0.05	240	49.78	76.41	74.97	0.12	8	2.5
0.1	262	50.37	76.46	75.02	0.1	3	1.5
0.15	276	51.18	76.87	75.44	0.06	1.25	0.6

distortions. On the other hand, in the present model, we have considered both Mn–O and La/K–O bond lengths to obtain the Mn–O, La/K–O and total force constants for strong electron–phonon interaction. The formulated effective interionic interaction potential includes the long-range Coulomb, vdW interaction and the short-range repulsive interaction up to second-neighbour ions within the Hafemeister and Flygare approach. The interionic interaction between a pair such as Mn–O and La/K–O enables us to find the total force constant with consistent Debye and Einstein temperatures.

In order to analyse the transport mechanism of the potassium-substituted manganites with $x = 0.05$, 0.1 and 0.15 in the intermediate-temperature ferromagnetic region below T_P, we begin with the electron–phonon interaction to discuss the metallic behaviour of $\rho(T)$. Figures 1, 2 and 3 illustrate the results of the temperature dependence of resistivity with the electron–phonon interaction from Eq. (31). The contributions of acoustic and optical phonon towards resistivity are clubbed and the resultant resistivity is exponential at low temperatures and nearly linear at high temperatures until the transition temperature. In the following calculations, we have used residual resistivity $\rho_0 \approx 0.12$, 0.1 and 0.06 Ω cm for $x = 0.05$, 0.1 and 0.15 [10]. The coefficients A_{ac} (A_{op}) as functions of doping concentration are shown in Table 3. It is noticed that the electron–phonon along with residual resistivity partially retraces the metallic resistivity behaviour of $La_{1-x}K_xMnO_3$ with ($x = 0.05$, 0.1 and 0.15) manganites and other temperature-dependent mechanisms such as electron–electron, and electron–magnon scattering should also be invoked.

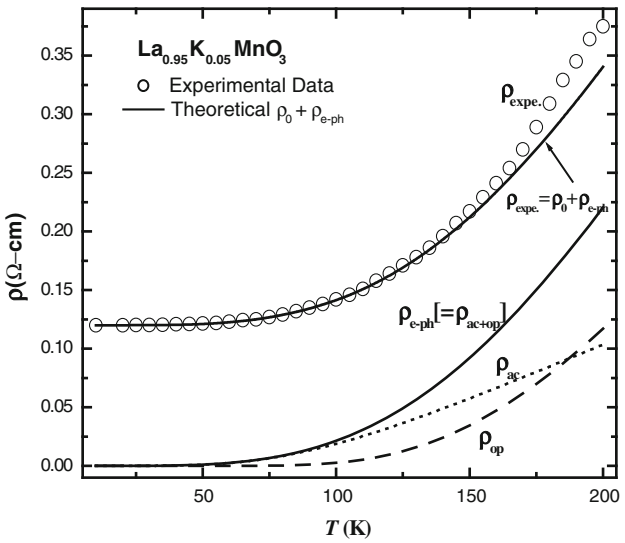

Fig. 1 Variation of $\rho_{e\text{-}ph}$ with temperature for $La_{0.95}K_{0.05}MnO_3$; the contribution of acoustic phonons ρ_{ac} as well of optical phonons ρ_{op} to the resistivity. The *solid line* represents best fit to the equation. $\rho = \rho_0 + \rho_{e\text{-}ph}$ (= $\rho_{ac} + \rho_{op}$). *Hollow circles* represent the experimental data [10]

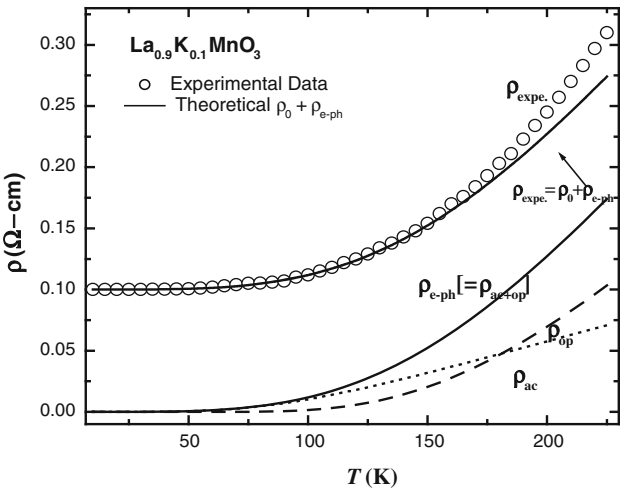

Fig. 2 Variation of $\rho_{e\text{-}ph}$ with temperature for $La_{0.9}K_{0.1}MnO_3$; the contribution of acoustic phonons ρ_{ac} as well of optical phonons ρ_{op} to the resistivity. The solid line represents best fit to the equation. $\rho = \rho_0 + \rho_{e\text{-}ph}$ (= $\rho_{ac} + \rho_{op}$). *Hollow circles* represent the experimental data [10]

It is noticed from the plot that the estimated ρ is lower than the reported data from $T \cong 150$ K for $La_{1-x}K_xMnO_3$ with ($x = 0.05$, 0.1 and 0.15) near the metal–insulator transition temperature (T_P). The difference between the measured ρ and calculated $\rho_{diff.}$ [= $\rho_{exp.} - \{\rho_0 + \rho_{e\text{-}ph}$ (= $\rho_{ac} + \rho_{op}$)}] is plotted in Fig. 4. A quadratic temperature dependence of $\rho_{diff.}$ is depicted at low temperature. The quadratic temperature contribution for resistivity is an indication of conventional inelastic electron–electron scattering.

The quadratic temperature dependence of $\rho_{diff.}$ is consistent with the earlier argument made by Urushibara et al. [15, 16]. The additional term due to electron–electron contribution was required in understanding the resistivity behaviour, as extensive attempts to it the data with residual resistivity and phonon resistivity were unsuccessful. It is noteworthy to comment that in conventional metals, the electron–electron contribution to the resistivity can at best be seen only at very low temperatures, due to its small magnitude in comparison with the phonon contribution. The existence of quadratic temperature dependence of resistivity over a wide temperature interval permits one to believe that the electron–electron scattering is also significant in determining the resistivity in manganites.

We again refer to Fig. 4, where a substantial deviation from the T^2-like behaviour and a rapid rise in $\rho_{diff.}$ are observed in the intermediate-temperature region ($185 < T < T_P$). We perform a similar set of exercises with the difference between the measured and calculated $\rho_{diff.}$ [= $\rho_{exp.} - \{\rho_0 + \rho_{e\text{-}ph}$ (= $\rho_{ac} + \rho_{op}$)}] beyond 185 K (plotted in Fig. 5). The $T^{4.5}$ temperature dependence of $\rho_{diff.}$ is depicted at higher temperature. The $T^{4.5}$ temperature

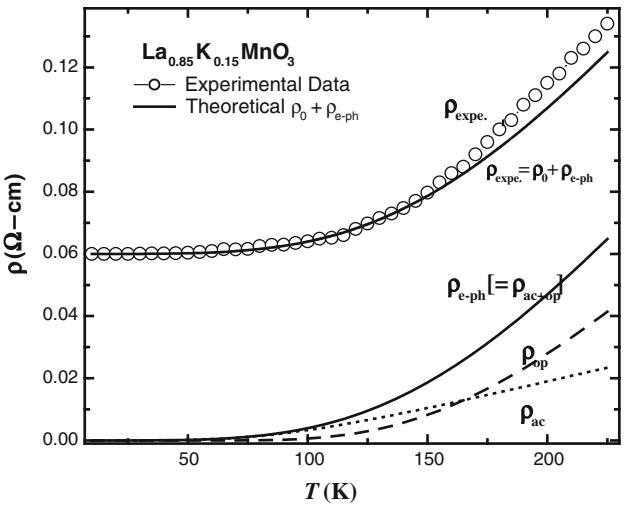

Fig. 3 Variation of $\rho_{\text{e-ph}}$ with temperature for $La_{0.85}K_{0.15}MnO_3$; the contribution of acoustic phonons ρ_{ac} as well of optical phonons ρ_{op} to the resistivity. The *solid line* represents best fit to the equation. $\rho = \rho_0 + \rho_{\text{e-ph}}$ $(= \rho_{ac} + \rho_{op})$. *Hollow circles* represent the experimental data [10]

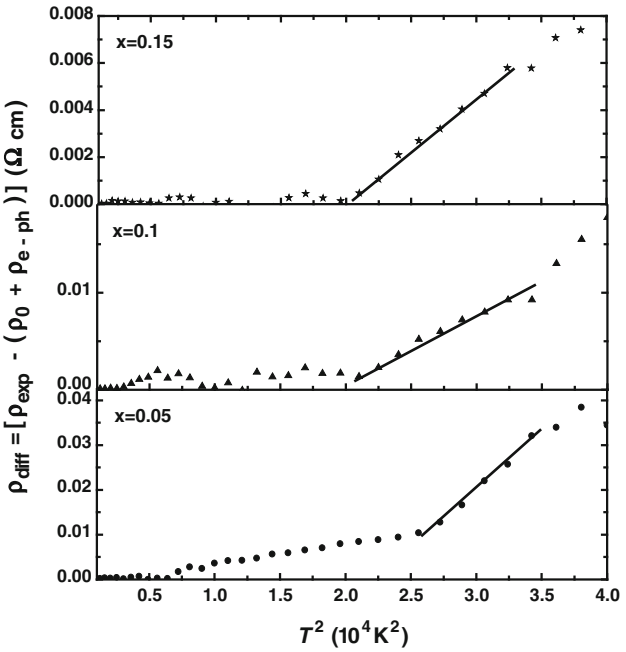

Fig. 4 Variation of $\rho_{\text{diff.}}$ $[= \rho_{\text{exp.}} - \{\rho_0 + \rho_{\text{e-ph}} (= \rho_{ac} + \rho_{op})\}]$ with T^2 of $La_{1-x}K_xMnO_3$ ($x = 0.05, 0.1, 0.15$)

contribution for resistivity is an indication of electron–magnon scattering. In the intermediate-temperature region ($185 < T < T_P$), the manganites appear to be normal metallic ferromagnet with the resistivity dominated by spin-wave scattering.

For hole-doped manganites, Snyder et al. [22] stressed that an additional $T^{4.5}$ contribution as a result of the electron–magnon scattering process is essential. In the recent past, we had also noticed that the spin-wave scattering in

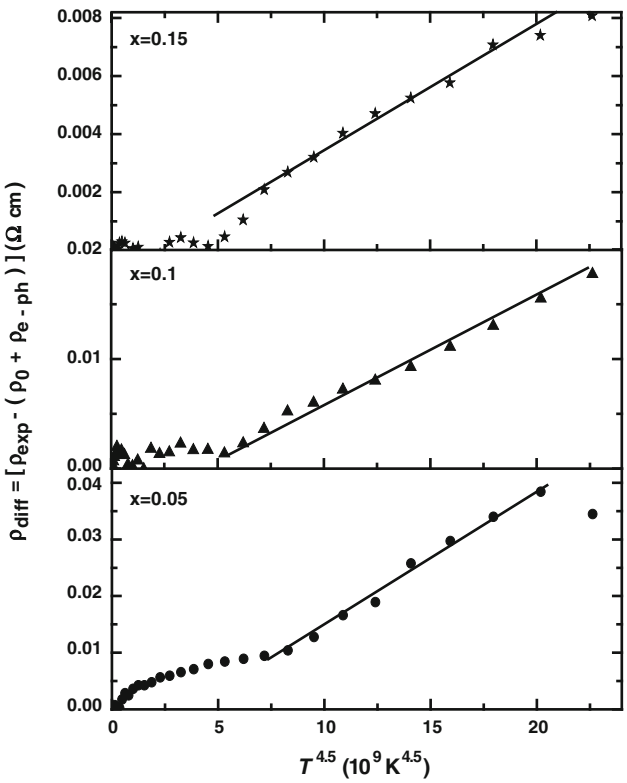

Fig. 5 Variation of $\rho_{\text{diff.}}$ $[= \rho_{\text{exp.}} - \{\rho_0 + \rho_{\text{e-ph}} (= \rho_{ac} + \rho_{op})\}]$ with $T^{4.5}$ of $La_{1-x}K_xMnO_3$ ($x = 0.05, 0.1, 0.15$)

the FM phase was important in discussing the electrical resistivity behaviour of $La_{0.67}Ca_{0.33}MnO_3$ [20]. We admit that in the higher temperature limit, the difference can be predicted linearly with $T^{4.5}$ in accordance with the electron–magnon scattering in the double-exchange process. The feature of $T^{4.5}$ temperature dependence of $\rho_{\text{diff.}}$ is consistent with the quantum theory of two-magnon scattering [18] and is valid for half-metallic ferromagnets. Consequently, besides electron–phonon and electron–electron interaction, another possibility for the changes in carrier density arose due to the presence of spin waves in the metallic system and is caused by spin-wave scattering.

We now address the metallic behaviour of doped manganites. If the high-frequency phonon modes are indeed strongly coupling with charge carriers, the effective mass of the carriers should be substantially enhanced. The Fermi energy and the corresponding density of states are conveniently obtained from the thermoelectric power results [10] using $\varepsilon_F = -\pi^2 k_B^2 T/[3|e|\cdot S_c^{\text{diff}}(T)]$ and $N(\varepsilon_F) = 3n_{3D}V/2\varepsilon_F$ (where n_{3D} is the three-dimensional charge carrier density which is obtained following $n_{3D}d^3 = 1$ and V is the unit cell volume). The density of states in turn yields the electronic specific heat coefficient using $\gamma = (\pi k_B)^2 N(\varepsilon_F)/3$ (see Table 4). It is noticed that the above values are consistent with the γ values in other hole-doped divalent manganites [43] and could not be compared due to a lack of

Table 4 The estimated electron parameters for $La_{1-x}K_xMnO_3$ ($x = 0.05, 0.1, 0.15$) manganites

x	ε_F (eV)	$N(\varepsilon_F) \times 10^{-19}$ (eV^{-1} cm^{-3})	γ (mJ mol^{-1} K^{-2})	m^*/m_E	$k_F \times 10^{-7}$ (cm^{-1})	$v_F \times 10^{-7}$ (cm s^{-1})	ω_p (eV)	$R_s \times 10^{-16}$ (s^{-1})	ℓ(Å)
0.05	1.52	3.10	2.722	2.959	3.750	1.46	1.248	3.819	0.03
0.1	1.81	2.63	2.303	2.504	3.749	1.72	1.356	3.759	0.04
0.15	2.03	2.34	2.049	2.229	3.748	1.94	1.437	2.532	0.07

experimental data on hole-doped monovalent manganites. The effective mass of the carrier along the conducting Mn–O plane is deduced from electronic specific heat coefficient γ, using $m^* = 3\hbar^2\pi\gamma d/k_B^2$.

The estimated electron parameters for $La_{1-x}K_xMnO_3$ with $x = 0.05, 0.1$ and 0.15 are the Fermi wave vector k_F, the Fermi velocity v_F and the plasma frequency ω_p as given in the Table 4. We stress that the effects induced by electron correlations and mass renormalizations by electron–electron interactions are crucial in magnetic systems such as doped manganites [44]. It is known that in conventional metals, electron–phonon scattering is mathematically identical to conventional impurity scattering and leads to resistivity proportional to $(v_F^2\ell)^{-1}$ where ℓ is the mean free path. The mean free path in this approximation is usually related to the Fermi velocity and is estimated following $\ell = v_F\tau$. We follow the Drude relation, $\tau^{-1} = \rho_0\omega_p^2/4\pi$, to obtain the scattering rate $R_s = \tau^{-1}$. The estimated values of R_s and ℓ are given in Table 4. We must mention that the residual resistance obtained for nominally the same compositions may vary significantly for different groups of compounds. It remains unclear whether ρ_0 only characterizes the sample's quality or if there is an intrinsic component in the residual resistivity [45]. For the Sr-doped manganites, the resistivity data in the crystalline films yield ρ_0 as low as 10^{-5} Ω cm and are in the range of typical metallic conductors [15, 16]. The deduced values of Fermi energy (ε_F) for $La_{1-x}K_xMnO_3$ with $x = 0.05, 0.1$ and 0.15 correspond to a narrow energy band. We notice that the K-doped lanthanum manganites are good metals as the product $\varepsilon_F\,\tau \sim 1$.

The electron correlations in view of the mass enhancement effect in narrow band materials are important in doped $LaMnO_3$. We notice that enhanced electron mass $m^*/m_E > 1$ in $La_{1-x}K_xMnO_3$ (see Table 4) leads to reduced plasma frequency and hence a reduced zero temperature elastic scattering rate in comparison to conventional metals. It is perhaps worth noticing that in hole-doped manganites, the scattering rate at low temperatures is of the order of 10^{15} s^{-1} [18]. Furthermore, the Mott–Ioffe–Regel criterion for metallic conductivity is valid, as the deduced mean free path is greater than the Mn–O bond length. The use of the BG expression in estimating the electron–phonon contributions is thus validated as the product $k_F\ell \sim 1$.

The monovalent K-doped manganites thus illustrate metallic behaviour below the metal–insulator transition temperature T_P. The T_P increases with the K doping concentration. With increased doping, the monovalent K-doped manganites behave as a good metal, and this is attributed to the fact that there are twice as many Mn^{4+} ions as there are K ions and each of these Mn^{4+} will contribute a hopping hole.

We must refer to the work of Egilmez et al. [46] who incorporate the effects of the grain boundary-induced lattice disorder on the resistivity in $Sm_{0.55}Sr_{0.45}MnO_3$ at temperatures near the metal–insulator transition. The low-temperature resistivity data ($T \leq 75$ K) of the SmSrMnO were successfully fitted using the relation $\rho = \rho_0 + \rho_2 T^2 + \rho_5 T^5$ with ρ_0 as the residual resistivity and ρ_2 and ρ_5 as the electron–electron and the electron–phonon scattering coefficients, respectively. It is further noticed that in this temperature range, the disorder does not affect the temperature dependence of ρ; however, it causes an increase in the coefficients ρ_0, ρ_2 and ρ_5 by two orders of magnitude.

In contrast to electron–phonon scattering as the source of resistivity in the FM metallic state, the angle-resolved photoemission spectroscopy data for the bilayer manganite $La_{1.2}Sr_{1.8}Mn_2O_7$ identify a coherent polaronic metallic ground state below the metal–insulator transition [47]. The FM state is a polaronic metal with a strong anisotropic character of the electronic excitations, strikingly similar to the pseudogap phases in heavily underdoped cuprate high-temperature superconductors such as Bi 2212. A strong mass enhancement and a small renormalization factor are found to account for the metallic properties [48]. The temperature dependence of resistivity in the metallic state is intimately related to polaronic metallic ground state, and the insulator-to-metallic state can be attributed to the polaron coherence condensation process acting in concert with the double-exchange mechanism. We may comment that the present theory finds an enhanced mass of holes as a carrier ($m^*/m_e > 1$ for $La_{1-x}K_xMnO_3$ with $x = 0.05, 0.1, 0.15$) from the electronic specific heat coefficient to validate the Mott–Ioffe–Regel criterion. However, a detailed analysis is further required to understand the polaronic metallic state in the ferromagnetic phase and the condensation process analogous to underdoped cuprate high-temperature superconductors. We shall address this issue in the near future.

Let us now discuss the semiconducting behaviour of the resistivity data in the high-temperature region and the

Table 5 Parameters obtained from the fitting of experimental data using VRH and SPC models

	T_0 10^6 (K)	$N(\varepsilon_F)$ 10^{20} (eV^{-1} cm^{-3})	D 10^{-3} (cm^2 s^{-1})	ρ_{os} 10^{-5}(Ω cm K^{-1})	E_p (meV)
$x = 0.05$	2.69	4.63	6.13	9.256	63.7
$x = 0.1$	2.03	6.10	6.22	8.749	61.9
$x = 0.15$	2.00	6.20	6.33	7.700	52.9

paramagnetic semiconducting state ($T > T_P$). We have computed the temperature-dependent resistivity of $La_{1-x}K_xMnO_3$ with ($x = 0.05$, 0.1, 0.15) using the VRH and adiabatic SPC models. Keep in mind that the charge carrier motion is faster than the lattice vibrations in the adiabatic regime and hence the nearest-neighbour hopping of a small polaron leads to mobility with a thermally activated form.

We shall first discuss the VRH model for carrier conduction. Originally, in the VRH theory, there was competition between the potential energy and the hopping distance of electrons. Figure 6 show the plots of ln $\sigma \sim T^{-1/4}$ revealing good concurrence with the VRH model [Eq. (32)]. The values of fitting parameters obtained from the fit of the high-temperature resistivity of $La_{1-x}K_xMnO_3$ with ($x = 0.05$, 0.1, 0.15) by the VRH model are given in Table 5. The fitted value of T_0 and the localisation length or the average hopping distance {$a = 4.6$ Å [21]} yield the density of states at the Fermi level, $N(\varepsilon_F)$, of the order of 10^{20} eV^{-1} cm^{-3}. The above sets of values are consistent with the fitting parameters for $Nd_{0.33}Ln_{0.34}Sr_{0.33}MnO_3$ [49].

To cross-check, we use the thermoelectric power measurement to calculate experimental value of the density of states at the Fermi level [43]. The deduced density of states $N(\varepsilon_F) \cong 3.109 \times 10^{19}$, 2.63×10^{19} and 2.34×10^{19} eV^{-1} cm^{-3} for $La_{1-x}K_xMnO_3$ with ($x = 0.05$, 0.1 and 0.15). We comment that the value of density of states at the Fermi level obtained from the semiconducting resistivity fit using VRH is higher by an order as obtained from the thermoelectric power measurements. This unphysical result leads us to argue that the VRH model is not the proper choice to describe resistivity behaviour in the high-temperature region $T > T_P$ for $La_{1-x}K_xMnO_3$ with ($x = 0.05$, 0.1 and 0.15). It was stressed by Mott and Davies [15, 16] that the VRH model is applicable only for the temperature region ($T_P < T < \theta_D/2$) in doped semiconductors.

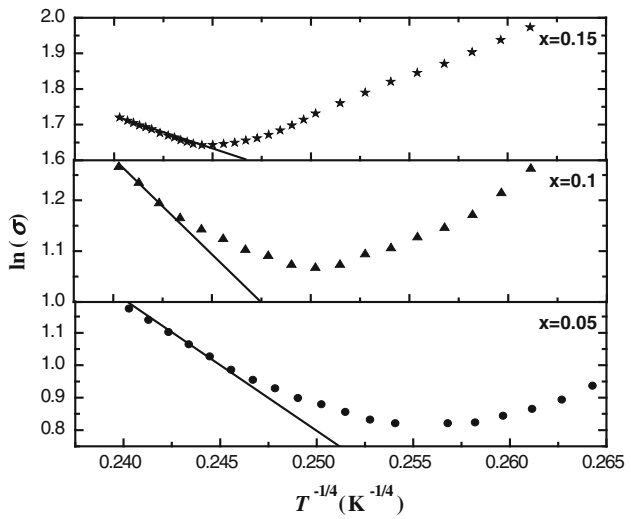

Fig. 6 Plots of ln(σ) vs. $T^{-1/4}$ of $La_{1-x}K_xMnO_3$ ($x = 0.05$, 0.1, 0.15) samples. The *solid line* represents best fit to the equation $\sigma = \sigma_0 \exp(-T_0/T)^{1/4}$. *Symbols* are the experimental data taken from [10]

The above is true for hole-doped monovalent manganites $La_{1-x}K_xMnO_3$ with ($x = 0.05$, 0.1 and 0.15) with $T_P \cong 240$, 262 and 276 K and $\theta_D \cong 582$, 589 and 598 K. In the passing, we must refer to Viret and coworkers who earlier stressed that the above discrepancy in the density of states at the Fermi level might be due to spin-dependent potential in doped manganites [21]. The above results are consistent with previous work on $La_{1-x}Na_xMnO_3$, $La_{1-x}Ba_xMnO_3$ ($x = 0.3$) and other doped manganites [37–41, 50–53]. In strongly correlated electron systems such as mixed-valent manganites, carrier hopping is always of a variable-range type at low temperature, as at low temperatures, the thermal energy (k_BT) is insufficient to allow electrons to hop to their nearest neighbours. However, electrons conveniently hop to farther neighbours to find a smaller potential difference. Thus, there is a competition between the potential energy difference and the distance that electrons can hop. On the other hand, at higher temperatures, the electron conduction is due to the activation above the mobility edge.

We have further used the adiabatic SPC model for the analysis of resistivity behaviour for high temperature. Charge carriers in the insulating region, above T_P, are not itinerant and transport properties are governed by thermally activated carriers (polarons) [22]. The conductivity in the high-temperature ($T > T_P$) PM-insulating state is dominated by the hopping motion of self-trapped small polarons [24]. To elucidate the nature of the charge transport mechanism in this high-temperature region, ln(ρ/T) has been plotted as a function of $1/T$ in Fig. 7. The good linear fits reveal that the conduction in the PM semiconducting region obeys the small polaron-hopping model, and the activation energy obtained from fitting is given in Table 5.

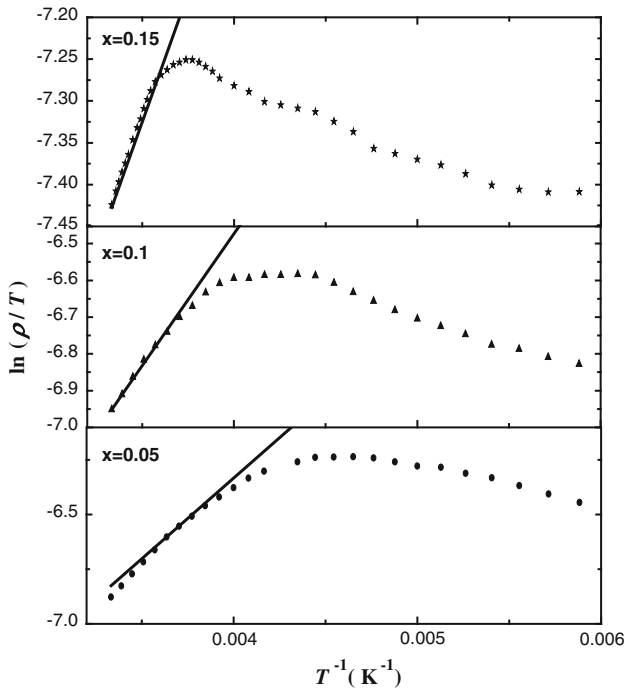

Fig. 7 Variation of $\ln(\rho/T)$ vs. inverse temperature (T^{-1}) of $La_{1-x}K_xMnO_3$ ($x = 0.05, 0.1, 0.15$) samples. The *solid line* represents the best fit to the equation $\rho = \rho_{os}T \exp(E_P/k_BT)$. *Symbols* are the experimental data taken from [10]

The decrease in E_p is also attributed to improvement of the grain surface state caused by the K addition.

We have first determined the diffusion coefficient using the lattice constant; the longitudinal optical phonon frequency and polaron formation energy are listed in Table 5. The best-fitting value of E_p is consistent with the earlier reported values of polaron formation energy of ranges from 58 to 170 meV in $La_{0.67}A_{0.33}MnO_3$ (A = Li, Na, K and Rb) [54]. The value of ρ_{os} is found to decrease with the increased K doping concentration, which implies an increase in the carrier density. The fact that E_p gradually decreases for higher doping is due to the phonon softening effect on carrier transport owing to Jahn–Teller distortions in the $La_{1-x}K_xMnO_3$. Henceforth, above T_P, the Jahn–Teller-type distortion present in the unit cell traps the charge carriers and gives rise to polarons. Hence, above T_P, the resistivity shows polaronic-type behaviour. With these facts, we state that the SPC model is only plausible for the higher temperature resistivity behaviour ($T > \theta_D/2$).

Conclusion

Either double-exchange mechanisms or small polarons have primarily described in the physics of manganites. The behaviour of electrical resistivity in doped manganites needs further clarification. The reported behaviour of electrical resistivity in K-doped manganites is analysed in the framework of the additional model of electron–phonon interaction using the model phonon spectrum consisting of two parts: an acoustic branch of Debye type and optical mode with characteristic Einstein temperature. Deduced values of Debye and Einstein temperatures from the model potential with the long-range Coulomb, vdW interaction and the short-range repulsive interaction up to second-neighbour ions within the Hafemeister and Flygare approach are consistent with Raman spectroscopy measurements. For the sake of simplicity, a single (longitudinal and transverse) optical phonon mode has been considered, with a flat dispersion relation.

The high-energy optical phonon yields a large contribution to the resistivity and is attributed to a significant optical phonon-hardening effect on carrier transport. It is noticeable that the contribution from acoustic and optical phonons together with the residual resistivity is smaller than experimental data. A clear straight line is depicted from $\sim$150 to $\sim$185 K temperature whilst plotting the difference as a function of power temperature indicative of electron–electron scattering. We further explore the role of electron–magnon scattering in the electrical transport mechanism. It is noticeable that the role of two-magnon scattering in the resistivity behaviour is prominent above 185 K. The incorporation of $T^{4.5}$ dependence is essential and consistently retraces the measured resistivity at higher temperatures. It is inferred from the above analysis that the electrical transport below T_P is dominated not only by electron–electron scattering but also by electron–magnon, presumably involving spin fluctuations of charge carriers.

We may comment that apart from the resistivity due to domain, grain boundary and the electron–phonon scattering, the electron–electron and electron–magnon scatterings are essential for a complete description of the metallic behaviour of $La_{1-x}K_xMnO_3$ with ($x = 0.05$, 0.1 and 0.15). The mean free path is comparable with the Mn–O bond length, and the products $k_F\ell \sim 1$ and $\varepsilon_F\ \tau \sim 1$ favour metallic conduction. Hence, it is appropriate to use the Bloch–Gruneisen expression in estimating the electron phonon contributions at $T < T_P$, and this is associated with the dynamic Jahn–Teller distortion, arising from the local lattice distortion due to the strong electron–phonon coupling.

The resistivity data of the semiconducting state at the high-temperature region, $T > T_P$, are analysed by using both the VRH and adiabatic SPC models. Deduced values of $N(\varepsilon_F)$ from resistivity fit using VRH are consistent with those obtained from thermoelectric power measurements. The SPC model with realistic physical parameters consistently retraces the semiconducting behaviour. The nearest-neighbour hopping of a small polaron leads to mobility with a thermally activated form and successfully retraced the

reported experimental curve in the paramagnetic phase. Above T_P, the Jahn–Teller-type distortion present in the unit cell traps the charge carriers and gives rise to polarons. Hence, above T_P, the resistivity shows polaronic-type behaviour.

To this end, the ferromagnetic metallic and paramagnetic semiconducting resistivity behaviour of $La_{1-x}K_xMnO_3$ manganites with ($x = 0.05$, 0.1 and 0.15) is investigated based on electron–phonon, electron–electron and electron–magnon as well SPC by deducing Debye, Einstein temperature, the diffusion coefficient and the polaron formation energy. The developed approach consistently explains the reported behaviour in the low-temperature regime ($T < T_P$) as well in the high-temperature regime ($T > T_P$). The scheme opted in the present study is so natural that it extracts only the essential contributions to describe the resistivity behaviour. As θ_D is about 582–600 K in this system, the use of BG expression and Debye model with $T < \theta_D$ is valid at low temperatures. Although we have provided a simple explanation of these effects, there is a clear need for good theoretical understanding of the resistivity behaviour in view of the formation of small polarons of magnetic origin in manganites.

References

1. Tokura Y, Nagaosa N (2000) Science 288:462
2. De Gennes PG (1960) Phys Rev 118:141
3. Millis AJ, Littlewood PB, Shraiman BI (1995) Phys Rev Lett 74:5144
4. Roy S, Guo YQ, Venkatesh S, Ali N (2001) J Phys Condens Matter 13:9547
5. Tetsuo S, Toshimasa H, Yoshiyuki I, Mitsuru I (1996) J Solid State Chem 124:250
6. Abrashev MV, Litvinchuk AP, Iliev MN, Meng RL, Popov VN, Ivanov VG, Chakalov RA, Thomsen C (1999) Phys Rev B 59:4146
7. Millis AJ, Shraiman Boris I, Mueller R (1996) Phys Rev Lett 77:175
8. Cengiz S, Gonzalo A, Elbio D (2007) Phys Rev Lett 98:127202
9. Rong Yu, Shuai D, Cengiz S, Gonzalo A, Elbio D (2008) Phys Rev B 77:214434
10. Soma D, Dey TK (2006) Physica B 381:280
11. Kumar S, Majumdar P (2005) Phys Rev Lett 94:136601
12. Kumar S, Majumdar P (2006) Phys Rev Lett 96:016602
13. Alexandrov AS, Guo-meng Z, Keller H, Lorenz B, Wang YS, Chu CW (2001) Phys Rev B 64:140404 (R)
14. Zhao GM, Smolyaninova V, Prellier W, Keller H (2000) Phys Rev Lett 84:6086
15. Urushibara A, Moritomo Y, Arima T, Asamitsu A, Kido G, Tokura Y (1995) Phys Rev B 51:14103
16. Mott NF, Davis EA (1979) Processes in non-crystalline material, 2nd edn. Oxford University Press, New York
17. Jaime M, Lin P, Salamon MB, Han PD (1998) Phys Rev B 58:R5901
18. Kubo K, Ohata N (1972) J Phys Soc Jpn 33:21
19. Alexandrov AS, Bratkovsky AM (1999) Phys Rev Lett 82:141
20. Varshney D, Kaurav N (2004) Eur Phys J B 40:129
21. Viret M, Ranno L, Coey JMD (1997) Phys Rev B 55:8067
22. Snyder GJ, Hiskes R, Dicarolis S, Beasley MR, Geballe TH (1996) Phys Rev B 53:14434
23. Jaime M, Hardner HT, Salamon MB, Rubinstein M, Dorsey P, Emin D (1997) Phys Rev Lett 78:951
24. Ang R, Lu WJ, Zhang RL, Zhao BC, Zhu XB, Song WH, Sun YP (2005) Phys Rev B 72:184417
25. Iliev MN, Abrashev MV, Lee H-G, Popov VN, Sun YY, Thomsen C, Meng RL, Chu CW (1998) Phys Rev B 57:2872
26. Granado E, Moreno NO, García A, Sanjurjo JA, Rettori C, Torriani I, Oseroff SB, Neumeier JJ, McClellan KJ, Cheong SW, Tokura Y (1998) Phys Rev B 58:11435
27. Tosi MP (1964) Solid State Phys 16:1
28. Hafemeister DW, Flygare WH (1965) J Chem Phys 43:795
29. Slater JC, Kirkwood JG (1931) Phys Rev 37:682
30. Varshney D, Kaurav N, Kinge R, Singh RK (2007) J Phys Condens Matter 19:236204
31. Varshney D, Shriya S, Varshney M, Khenata R (2012) Comput Mater Sci 61:158
32. Varshney D, Shriya S, Khenata R (2012) Mater Chem Phys 135:365
33. Varshney D, Shriya S, Varshney M (2012) Eur Phys J B 85:241
34. Gruneisen E (1933) Ann Phys (Leipz) 16:530
35. Millis AJ (1996) Phys Rev B 53:8434
36. Ederer C, Lin C, Millis AJ (2007) Phys Rev B 76:155105
37. Varshney D, Shaikh MW, Mansuri I (2009) J Alloys Compd 486:726
38. Varshney D, Mansuri I (2011) J Low Temp Phys 162:52
39. Varshney D, Dodiya N, Shaikh MW (2011) J Alloys Compd 509:7447
40. Varshney D, Kaurav N (2005) J Low Temp Phys 141:165
41. Varshney D, Mansuri I, Kaurav N (2007) J Phys Condens Matter 19:246211
42. Marzari N, Vanderbilti D (1997) Phys Rev B 56:12847
43. Ghivelder L, Castillo IA, Alford NM, Tomka GJ, Riedi PC, MacManus-Driscoll J, Hossain AK, Akther M, Cohen LF (1998) J Magn Magn Mater 189:274
44. Varshney D, Kaurav N (2004) Eur Phys J B 37:301
45. Quijada M, Cerne J, Simpson JR, Drew HD, Ahn KH, Millis AJ, Shreekala R, Ramesh R, Rajeswari M, Venkatesan T (1998) Phys Rev B 58:16093
46. Egilmez M, Chow KH, Jung J, Fan I, Mansour AI, Salman Z (2008) Appl Phys Lett 92:132505
47. Mannella N, Yang WL, Tanaka K, Zhou XJ, Zheng H, Mitchell JF, Zaanen J, Devereaux TP, Nagaosa N, Hussain Z, Shen ZX (2007) Phys Rev B 76:233102
48. Mannella N, Yang WL, Zhou XJ, Zheng H, Mitchell JF, Zaanen J, Devereaux TP, Nagaosa N, Hussain Z, Shen ZX (2005) Nature 438:474
49. Padmavathi K, Venkataiah G, Reddy PV (2007) J Magn Magn Mater 309:237
50. Varshney D, Choudhary D, Shaikh MW (2010) Comput Mater Sci 47:839
51. Varshney D, Choudhary D, Shaikh MW, Khan E (2010) Eur Phys J B 76:327
52. Varshney D, Dodiya N (2011) Mater Chem Phys 129:896
53. Shaikh MW, Varshney D (2012) Mater Chem Phys 134:886
54. Lakshmi YK, Venkataiah G, Vithal M, Reddy PV (2008) Phys B 403:3059